molecules

MDPI

*Article*

# Synergistic Enhancement of Electrocatalytic Oxygen Evolution via Photothermal Effect in NiFeS/$Cs_{0.32}WO_3$

**Ze Wang [1,†], Xin Zhang [1,†], Wucong Wang [1], Xiong Yang [1,2], Xinyu Song [1] and Shifeng Wang [1,*]**

[1] Key Laboratory of Plateau Oxygen and Living Environment of Xizang Autonomous Region and College of Science, Xizang University, Lhasa 850000, China; yangx@ustb.edu.cn (X.Y.)
[2] School of Energy and Environmental Engineering, University of Science and Technology Beijing, Beijing 100000, China
* Correspondence: wsf@utibet.edu.cn
† These authors contributed equally to this work.

## Abstract

Photothermal-assisted electrocatalysis is an effective approach to enhance the efficiency of the oxygen evolution reaction (OER), but the synergistic mechanism between the photothermal effect and the regulation of catalyst electronic structure remains unclear. This work reports the construction of NiFeS/$Cs_{0.32}WO_3$ heterostructures, which integrate interfacial electron transfer and localized surface plasmon resonance (LSPR)-induced photothermal effects to enhance OER performance. The $Cs_{0.32}WO_3$ component with hexagonal tungsten bronze structure exhibits strong absorption in the near-infrared region, attributed to LSPR (1100 nm to 2500 nm) and small polaron transition (780 nm to 1100 nm), endowing the NiFeS/$Cs_{0.32}WO_3$ composite with excellent photothermal conversion capability. Under 808 nm laser irradiation, the steady-state surface temperature of the heterostructure reaches 65.1 °C. X-ray photoelectron spectroscopy and ultraviolet photoelectron spectroscopy analyses reveal that spontaneous electron transfer from NiFeS to $Cs_{0.32}WO_3$ occurs at the heterostructure interface, thereby optimizing the electronic structure of active sites. Electrochemical measurements demonstrate that at a current density of 50 mA $cm^{-2}$, the NiFeS/$Cs_{0.32}WO_3$ composite exhibits an overpotential of 301 mV under near-infrared irradiation, representing a reduction of 53 mV compared to NiFeS under dark conditions. At a current density of 50 mA $cm^{-2}$, the photothermal enhancement effect of the NiFeS/$Cs_{0.32}WO_3$ composite is identified as the predominant contributor to the overall performance improvement. Nevertheless, the intrinsic interfacial effect associated with the heterojunction also plays a crucial role and makes a non-negligible contribution to the enhanced electrocatalytic activity. The Tafel slope decreases from 57.8 mV $dec^{-1}$ to 44.5 mV $dec^{-1}$ under near-infrared illumination, indicating accelerated OER kinetics. This work elucidates the mechanism of synergistic enhancement between heterostructure construction and photothermal effects, providing insights for the design of advanced photothermal electrocatalysts.

**Keywords:** oxygen evolution reaction; heterostructure; photothermal effect; NiFeS



Academic Editor: Isabella Natali Sora

Received: 28 May 2026
Revised: 27 June 2026
Accepted: 29 June 2026
Published: 2 July 2026



## 1. Introduction

The rapid depletion of fossil fuel reserves and the increasingly severe environmental deterioration caused by carbon emissions have driven global research into clean and renewable energy alternatives [1,2]. Hydrogen possesses an extremely high gravimetric energy density (approximately 120 MJ $kg^{-1}$) and produces only water as a combustion product,

making it a crucial energy carrier for achieving carbon neutrality [3,4]. Electrochemical water splitting driven by renewable electricity is one of the most promising approaches for sustainable hydrogen production, offering advantages such as high product purity, environmental friendliness, and scalability [5]. However, the large-scale application of this technology is still severely constrained by the sluggish intrinsic kinetics of the anodic oxygen evolution reaction (OER), which is a four-electron transfer process accompanied by the generation of multiple oxygen-containing intermediates (*OH, *O, *OOH) and substantial thermodynamic energy barriers [6,7]. Currently, iridium dioxide ($IrO_2$) and ruthenium dioxide ($RuO_2$), owing to their favorable electronic configurations and near-optimal binding energies with reaction intermediates, remain the benchmark electrocatalysts for OER [8]. Nevertheless, these noble metal oxides suffer from high cost, low crustal abundance, and poor long-term operational stability, severely limiting their practical application in large-scale commercial electrolyzers [9,10]. Therefore, developing earth-abundant transition metal-based electrocatalysts with competitive catalytic activity and durability has become an important research direction [11].

Among numerous candidate materials, nickel-iron-based compounds have attracted attention due to the strong synergistic interactions between Ni and Fe centers, where the incorporation of Fe can modulate the oxidation state of Ni and promote the formation of catalytically active oxyhydroxide species during OER [12]. Heterostructure construction for interfacial engineering has become an effective strategy to overcome the inherent limitations of single-component materials and enhance electrocatalytic performance [13,14]. At heterostructure interfaces, the contact between materials with different work functions spontaneously induces electron redistribution and forms a built-in electric field, which can effectively modulate the local electronic environment of catalytically active sites [15]. Interfacial charge transfer phenomena can optimize the d-band center position of transition metals, regulate the adsorption energies of OER intermediates, and reduce charge transfer resistance [16,17]. To date, numerous heterostructure architectures have been constructed to promote OER electrocatalysis, including Mott–Schottky contacts (Ru-$RuO_2$, Co/CoP) [13,17], semiconductor–semiconductor junctions ($NiS/MoS_2$, NiFe-LDH/NiS, $Ni_3Se_2$/NiSe) [18–20], and carbon-supported composite structures (Ni/$CeO_2$@N-CNFs, WN-Ni@N,P-CNT, Co-$Mo_2C$/CNx) [21–23].

Beyond the modification of catalysts themselves, the introduction of external energy fields represents a novel approach to break through the limitations of conventional catalytic performance [24]. Among various external stimuli, photothermal-assisted electrocatalysis has attracted extensive research as an energy-efficient enhancement strategy [25,26]. Light-absorbing materials generate localized surface heating upon irradiation, which thermodynamically reduces the required overpotential according to the Nernst equation and kinetically accelerates mass transfer and charge transfer processes [27,28]. Additionally, the localized heating effect facilitates the detachment of evolved gas bubbles from the electrode surface, maintaining effective accessibility to active sites during continuous operation [29]. Photothermal enhancement strategies have been successfully applied to numerous materials including nickel sulfides [29], nickel phosphides [30], cobalt-based compounds [31], MXenes [32], and plasmonic metal nanostructures [33], capable of operating under solar or near-infrared (NIR) irradiation [34–37]. Cesium tungsten bronze ($Cs_{0.32}WO_3$) is a plasmonic semiconductor with exceptional near-infrared absorption properties [38]. The hexagonal tungsten bronze structure of $Cs_{0.32}WO_3$ features hexagonal tunnel channels that accommodate $Cs^+$ ions, which act as electron donors to generate abundant free carriers, producing localized surface plasmon resonance (LSPR) absorption in the range of 1100 to 2500 nm [38,39]. Furthermore, small polaron transitions between adjacent $W^{5+}$ and $W^{6+}$sites contribute additional absorption in the spectral region from 780 nm to 1100 nm [39]. The

dual absorption mechanisms endow $Cs_{0.32}WO_3$ with excellent photothermal conversion efficiency under near-infrared irradiation.

This work reports the rational design and synthesis of NiFeS/$Cs_{0.32}WO_3$ heterostructures, which integrate heterostructure-mediated electronic modulation with LSPR-enhanced photothermal effects to achieve efficient OER electrocatalysis. The composite catalyst was prepared via a facile two-step solvothermal method, and interfacial electron transfer from NiFeS to $Cs_{0.32}WO_3$ was elucidated using X-ray photoelectron spectroscopy (XPS) and ultraviolet photoelectron spectroscopy (UPS) analyses. UV-vis-NIR diffuse reflectance spectroscopy and infrared thermal imaging demonstrated that the heterostructure possesses excellent photothermal conversion performance, achieving a steady-state temperature of 65.1 °C under near-infrared irradiation. Importantly, quantitative decoupling analysis was employed to separately determine the contributions of heterostructure effects and photothermal effects to the overall OER enhancement. To place the present work in a broader academic context, the photothermally enhanced OER performance of the NiFeS/$Cs_{0.32}WO_3$ composite was systematically compared with recently reported state-of-the-art systems, including NiFe-LDH/plasmonic metal composites [40] and transition metal sulfide/oxide heterostructures [41]. Compared with NiFe-LDH-based system, the present catalyst exhibits a low Tafel slope of 44.5 mV $dec^{-1}$. Moreover, the incorporation of NiFeS endows the catalyst with superior intrinsic electrical conductivity, thereby facilitating efficient charge transfer during the OER process. In comparison with transition metal sulfide/oxide heterostructures, the proposed NiFeS/$Cs_{0.32}WO_3$ architecture features a simpler structural design while achieving competitive photothermal enhancement, thus avoiding the complexity associated with multi-heterojunction interface engineering. This work provides mechanistic insights and design strategies for the development of advanced photothermal electrocatalysts.

## 2. Results and Discussion

X-ray diffraction (XRD) was employed to analyze the crystal structure and phase composition of the prepared samples. Figure 1 shows the XRD patterns of $Cs_{0.32}WO_3$, NiFeS, and NiFeS/$Cs_{0.32}WO_3$-60 mg composite. The diffraction pattern of NiFeS shows that its diffraction peaks match well with the standard cards of $C_8H_6Fe_2O_7$ (PDF#00-033-1724), $Fe_{0.65}Ni_{0.35}$ (PDF#04-002-8942), and $Ni_3S_2$ (PDF#97-003-6338), indicating that NiFeS is a multiphase composite material with successful incorporation of metal sulfides. Among these phases, $Ni_3S_2$ belongs to the rhombohedral crystal system with lattice parameters of a = b = c = 4.08 Å and $\alpha = \beta = \gamma = 89.42°$. The characteristic diffraction peaks appearing at $2\theta = 21.8°$, 31.1°, 37.8°, 44.5°, and 54.8° correspond to the (100), ($\bar{1}$10), (111), (200), and (211) crystal planes of $Ni_3S_2$, respectively. The formation of the $C_8H_6Fe_2O_7$ phase is attributed to the coordination interaction between terephthalic acid and iron ions during the solvothermal process, while the formation of the $Fe_{0.65}Ni_{0.35}$ alloy phase results from the partial reduction of $Fe^{3+}$ and $Ni^{2+}$ under reducing atmosphere. The diffraction pattern of $Cs_{0.32}WO_3$ is in excellent agreement with the standard card PDF#01-083-1334, exhibiting a typical hexagonal tungsten bronze structure (a = b = 7.4116 Å, c = 7.5981 Å, $\alpha = \beta = 90°$, $\gamma = 120°$). The characteristic peaks at 23.5°, 27.4°, 27.9°, 36.7°, and 49.3° belong to the (002), (102), (200), (202), and (220) crystal planes, respectively. The sharp and intense diffraction peaks indicate that the prepared $Cs_{0.32}WO_3$ possesses high crystallinity. In the diffraction pattern of the NiFeS/$Cs_{0.32}WO_3$ composite, in addition to retaining all the characteristic diffraction peaks of NiFeS, the characteristic diffraction peaks of $Cs_{0.32}WO_3$ are clearly observed at $2\theta = 23.4°$, 27.3°, 27.8°, 33.8°, and 36.7°, confirming the successful compositing of the two materials. It is noteworthy that the diffraction peaks of $Cs_{0.32}WO_3$ in the composite are slightly shifted to lower angles compared

to the pure phase sample, which may be attributed to the slight lattice expansion of $Cs_{0.32}WO_3$ caused by interfacial interactions between NiFeS and $Cs_{0.32}WO_3$.

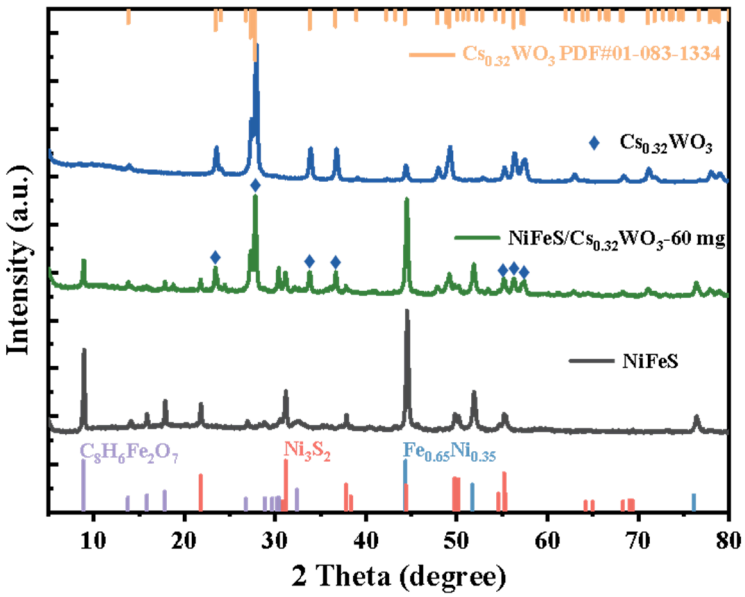


**Figure 1.** XRD patterns of $Cs_{0.32}WO_3$, NiFeS, and NiFeS/$Cs_{0.32}WO_3$-60 mg composite.

Transmission electron microscopy (TEM) was employed to characterize the morphology and microstructure of the prepared samples. As shown in Figure 2a, NiFeS exhibits a flower-like structure assembled from ultrathin nanosheets, which are interwoven and stacked to form an abundant porous network structure that is beneficial for increasing the specific surface area of the material and providing more active sites. Figure 2b shows the TEM image of $Cs_{0.32}WO_3$, revealing that $Cs_{0.32}WO_3$ exhibits a regular polyhedral morphology with well-defined edges, indicating good crystallinity. Figure 2c,f present TEM images of the NiFeS/$Cs_{0.3}$2$WO_3$-60 mg composite, showing that $Cs_{0.32}WO_3$ polyhedral particles are distributed within the NiFeS nanosheet network, forming intimate contact interfaces between the two phases, which is favorable for rapid charge transfer at the interface. To further elucidate the crystal structure of the samples, high-resolution transmission electron microscopy (HRTEM) analysis was conducted. Figure 2d shows the HRTEM image of $Cs_{0.32}WO_3$, where the measured lattice spacing is 0.34 nm, corresponding to the (102) crystal plane of $Cs_{0.32}WO_3$. Figure 2e displays the HRTEM image of the NiFeS/$Cs_{0.32}WO_3$ composite, where lattice fringes of different phases can be observed within the same field of view. Among them, the lattice fringes with spacings of 0.24 nm and 0.19 nm correspond to the (111) and (200) crystal planes of $Ni_3S_2$, respectively, with a measured interplanar angle of 55.9°, which is very close to the theoretical value of 55.2°, further confirming the presence of the $Ni_3S_2$ phase. Additionally, the lattice fringe with a spacing of 0.31 nm is attributed to the (200) crystal plane of $Cs_{0.32}WO_3$, which is slightly smaller than the standard d-spacing of pure $Cs_{0.32}WO_3$ (0.32 nm), echoing the observation from XRD analysis of diffraction peak shifts to lower angles and slight lattice expansion in the composite, indicating interfacial interactions between NiFeS and $Cs_{0.32}WO_3$. The above HRTEM results corroborate the XRD analysis, fully confirming the multiphase coexistence characteristics in the composite material. Figure 2g shows the energy-dispersive X-ray spectroscopy (EDS) elemental mapping images of the NiFeS/$Cs_{0.32}WO_3$ composite. The results reveal that Ni, Fe, and S elements are predominantly distributed in the nanosheet regions, while Cs, W, and O elements are mainly concentrated in the polyhedral particle regions, consistent with the morphological features observed by TEM. EDS line scanning results (Figure S1)

further reveal the spatial distribution patterns of each element, showing that Ni and Fe signals exhibit distinctly complementary distribution characteristics with Cs and W signals, confirming the successful construction of the NiFeS/$Cs_{0.32}WO_3$ heterostructure.

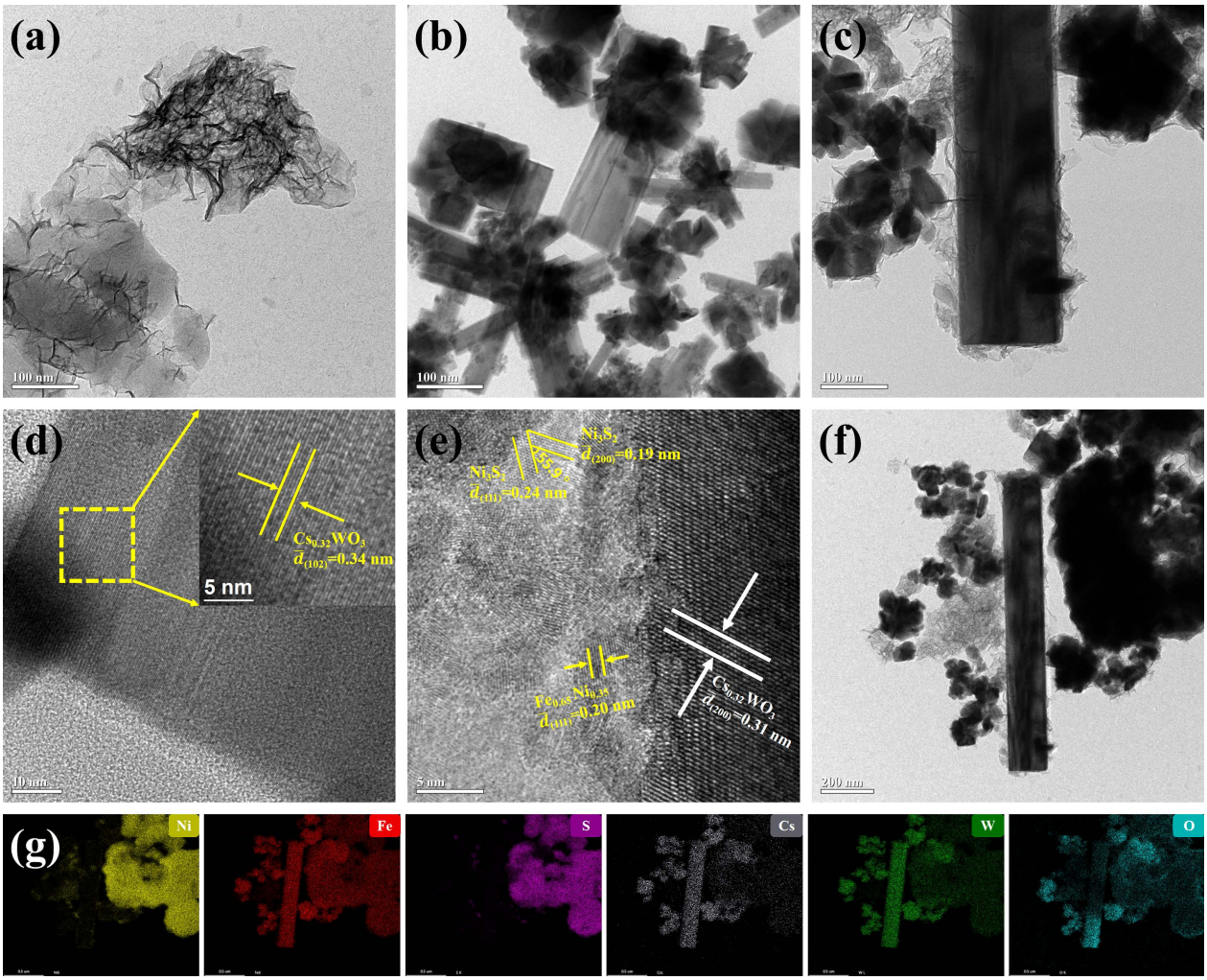


**Figure 2.** (**a**) TEM image of NiFeS; (**b**,**d**) TEM and HRTEM images of $Cs_{0.32}WO_3$; (**c**,**f**) TEM images and (**e**) HRTEM images of NiFeS/$Cs_{0.32}WO_3$-60 mg composite; (**g**) EDS elemental mapping images of NiFeS/$Cs_{0.32}WO_3$-60 mg composite.

The elemental composition and chemical states of the samples were characterized by X-ray photoelectron spectroscopy (XPS) (Figure 3). Figure 3a shows the XPS survey spectra of NiFeS, $Cs_{0.32}WO_3$, and NiFeS/$Cs_{0.32}WO_3$-60 mg composite. Characteristic peaks of Ni, Fe, S, O, and C elements were detected in the NiFeS sample, while the $Cs_{0.32}WO_3$ sample exhibited characteristic signals of Cs, W, and O elements. In the survey spectrum of the NiFeS/$Cs_{0.32}WO_3$-60 mg composite, characteristic peaks of Ni 2p, Fe 2p, S 2p, Cs 3d, W 4f, and O 1s were simultaneously observed, confirming the successful compositing of the two materials, consistent with XRD and EDS analysis results. To further elucidate the chemical states of each element and interfacial electronic interactions, high-resolution XPS analysis was performed on the main elements. As shown in Figure 3b, in the Ni 2p spectrum of the NiFeS sample, the peaks located at 855.8 and 873.4 eV correspond to the $2p^{3/2}$ and $2p^{1/2}$ orbitals of $Ni^{2+}$, respectively, while the peaks at 857.7 and 875.3 eV are attributed to $Ni^{3+}$, accompanied by satellite peaks (Sat.). Additionally, the characteristic peak of the Ni-S bond can be observed at 852.8 eV, indicating the presence of nickel sulfide. In the Fe 2p spectrum (Figure 3c), the peaks located at 712.9 and 725.3 eV in the NiFeS

sample correspond to the $2p^{3/2}$ and $2p^{1/2}$ orbitals of $Fe^{3+}$, respectively, while the peaks at 709.9 and 722.7 eV are attributed to $Fe^{2+}$. In comparison, in the NiFeS/$Cs_{0.32}WO_3$ composite, the Fe $2p^{3/2}$ peak shifts toward higher binding energy by 0.72 eV, while this region also overlaps with the Cs $3d^{3/2}$ and Cs $3d^{5/2}$ signal peaks. The positive shift in Fe 2p binding energy indicates a decrease in electron cloud density around Fe, signifying electron transfer from NiFeS to $Cs_{0.32}WO_3$. The analysis results of the O 1s spectrum are shown in Figure 3d. The O 1s spectrum of NiFeS can be fitted into three peaks: the peak at 530.1 eV corresponds to metal–oxygen bonds (M-O), the main peak at 531.4 eV is attributed to metal–hydroxyl bonds (M-OH), and the peak at 533.8 eV corresponds to adsorbed water ($H_2O$). For the Cs 3d spectrum (Figure 3e), the peaks located at 723.9 and 737.9 eV in the NiFeS/$Cs_{0.32}WO_3$ composite correspond to the $3d^{5/2}$ and $3d^{3/2}$ orbitals of Cs 3d, respectively. Compared to the pure NiFeS sample, the Cs 3d orbital peak shifts toward lower binding energy by 0.14 eV, indicating an increase in electron cloud density around Cs, signifying that $Cs_{0.32}WO_3$ has received electrons from NiFeS. From the W 4f spectrum (Figure 3f), it can be seen that the W 4f spectrum of the NiFeS/$Cs_{0.32}WO_3$ composite is fitted into two sets of spin–orbit splitting peaks, where the peaks at 35.6 and 37.7 eV correspond to the $4f^{7/2}$ and $4f^{5/2}$ orbitals of $W^{6+}$, while the peaks at 34.4 and 36.7 eV are attributed to $W^{5+}$. The presence of $W^{5+}$ results from the intercalation of $Cs^+$ into the $WO_3$ lattice, causing partial reduction of $W^{6+}$, which is a typical characteristic of cesium tungsten bronze. Compared to the pure NiFeS sample, the W 4f peak in the composite shifts toward lower binding energy by 0.26 Ev, further confirming electron transfer from NiFeS to $Cs_{0.32}WO_3$. According to the above XPS analysis results, significant electron transfer occurs at the NiFeS/$Cs_{0.32}WO_3$ interface, with electrons transferring from NiFeS to $Cs_{0.32}WO_3$. This interfacial electronic interaction can modulate the electronic structure of the catalyst, optimize the adsorption energies of OER intermediates, and thereby enhance electrocatalytic activity.

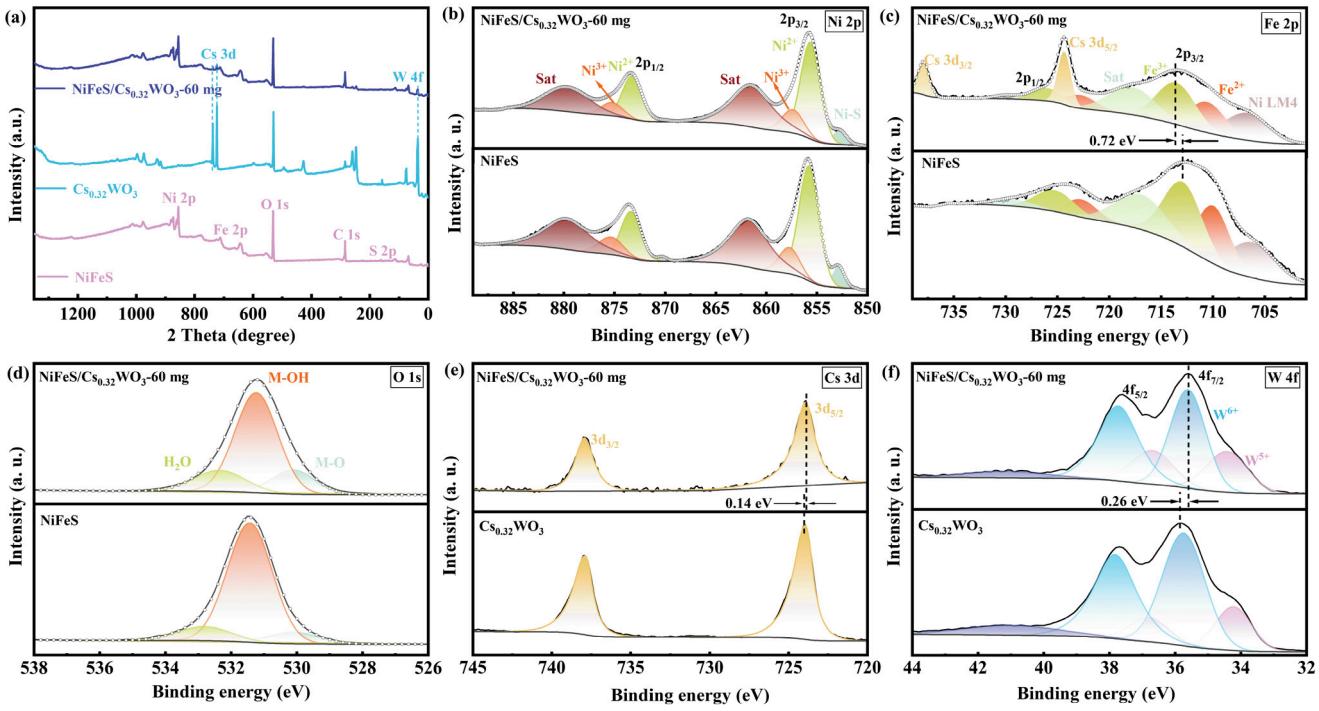


**Figure 3.** XPS spectra of NiFeS, $Cs_{0.32}WO_3$, and NiFeS/$Cs_{0.32}WO_3$-60 mg: (**a**) survey spectra; (**b**) Ni 2p; (**c**) Fe 2p; (**d**) O 1s; (**e**) Cs 3d; (**f**) W 4f.

To investigate the effect of $Cs_{0.32}WO_3$ incorporation on the optical properties of the composite, the samples were characterized using UV–visible diffuse reflectance spectroscopy (UV-vis DRS). As shown in Figure 4a, NiFeS exhibits strong absorption in the ultraviolet region of 200–400 nm, but its absorption capacity decreases sharply in the visible and near-infrared regions. In comparison, the NiFeS/$Cs_{0.32}WO_3$-60 mg composite exhibits higher absorption intensity across the entire tested wavelength range, with particularly significant enhancement in the near-infrared region. This is attributed to the localized surface plasmon resonance (LSPR) effect of free electrons in the unique hexagonal tungsten bronze structure of $Cs_{0.32}WO_3$, which endows it with strong light absorption capability in the near-infrared region. To more intuitively evaluate the photothermal conversion performance of the samples, an 808 nm near-infrared laser was used to irradiate the samples, and the temperature changes in the materials were monitored in real-time using an infrared thermal imaging camera. Figure 4b shows the infrared thermal images of NiFeS, $Cs_{0.32}WO_3$, and NiFeS/$Cs_{0.32}WO_3$-60 mg composite under different laser irradiation times. From the thermal images, it can be observed that all three samples exhibit significant temperature rise under laser irradiation. Under the same irradiation time, $Cs_{0.32}WO_3$ and the NiFeS/$Cs_{0.32}WO_3$ composite demonstrate faster heating rates, with their thermal imaging regions showing orange-red color (representing higher temperatures) earlier, while the heating rate of NiFeS is relatively slower. As the irradiation time extends to 50 s, the central regions of both $Cs_{0.32}WO_3$ and the NiFeS/$Cs_{0.32}WO_3$ composite reach higher temperatures and display bright white color, while the central temperature of NiFeS is relatively lower, intuitively demonstrating that samples containing $Cs_{0.32}WO_3$ possess superior photothermal conversion capability. (The temperature data were obtained from surface temperature measurements of dry powder samples in air. These results are intended solely to qualitatively demonstrate the photothermal heating capability of the $Cs_{0.32}WO_3$ component and do not represent the actual temperature at the electrode/electrolyte interface under OER operating conditions.) Figure 4c shows the temperature versus time curves of the three samples under 808 nm laser irradiation. All samples exhibit rapid temperature increase at the onset of irradiation (0–40 s), followed by gradual approach to equilibrium. In terms of steady-state temperature, $Cs_{0.32}WO_3$ exhibits the most excellent photothermal conversion performance; the NiFeS/$Cs_{0.32}WO_3$-60 mg composite ranks second with an equilibrium temperature of approximately 65 °C; meanwhile, pure NiFeS has an equilibrium temperature of only about 60 °C. The inset shows a comparison of average temperatures during the 100–200 s period, where the average temperature of NiFeS is 60.4 °C, while that of the NiFeS/$Cs_{0.32}WO_3$-60 mg composite reaches 65.1 °C, with a temperature difference of approximately 4.7 °C. This indicates that the incorporation of $Cs_{0.32}WO_3$ enhances the photothermal conversion capability of the composite. From the above results, it can be seen that $Cs_{0.32}WO_3$, owing to its excellent near-infrared light absorption and photothermal conversion efficiency, can serve as an efficient photothermal component incorporated into the NiFeS system. Under illumination, the localized thermal effect generated in the composite can increase the electrolyte temperature, accelerate mass transfer processes at the electrode/electrolyte interface, reduce reaction activation energy, and thereby potentially achieve photothermal-assisted enhancement of electrocatalytic oxygen evolution performance.

To evaluate the electrocatalytic oxygen evolution reaction (OER) performance of the catalysts, tests were conducted in 1 M KOH electrolyte using a standard three-electrode system, and the catalytic activities under dark and photothermal conditions were compared. Figure 5a shows the linear sweep voltammetry (LSV) curves of NiFeS and NiFeS/$Cs_{0.32}WO_3$ composites with different $Cs_{0.32}WO_3$ additions under dark and photothermal conditions. It can be seen that the LSV curves of all samples shift toward lower potentials under photothermal conditions, indicating that the photothermal effect can promote OER kinetics. At

the same current density, the NiFeS/$Cs_{0.32}WO_3$-60 mg composite exhibits the most excellent catalytic activity. To quantitatively analyze the respective contributions of heterostructure construction and photothermal effect to OER performance enhancement, systematic comparison of potentials under different conditions was conducted at a benchmark current density of 50 mA $cm^{-2}$. As shown in Figure 5a, the potential required for NiFeS to reach 50 mA $cm^{-2}$ under dark conditions is 1.584 V. After introducing $Cs_{0.32}WO_3$ to construct the heterostructure, the potential of the NiFeS/$Cs_{0.32}WO_3$-60 mg composite under dark conditions decreases to 1.562 V, a reduction of 22 mV, which can be attributed to the electron transfer effect at the heterostructure interface optimizing the electronic structure of the catalyst. Upon further introduction of the photothermal effect, the potential of the NiFeS/$Cs_{0.32}WO_3$-60 mg composite under photothermal conditions further decreases to 1.531 V vs. RHE, a reduction of 31 mV compared to dark conditions, which results from the localized thermal effect generated by the photothermal conversion of $Cs_{0.32}WO_3$. Therefore, the NiFeS/$Cs_{0.32}WO_3$-60 mg composite under photothermal conditions exhibits a potential reduction of 53 mV compared to NiFeS under dark conditions. The enhanced overall performance of the NiFeS/$Cs_{0.32}WO_3$ composite is primarily attributed to its photothermal enhancement effect, whereas the intrinsic interfacial effects arising from the heterojunction also contribute significantly and cannot be neglected. Quantitative decoupling analysis clearly demonstrates that heterostructure construction and photothermal assistance have synergistic enhancement effects on electrocatalytic performance improvement. As a control, the potential of NiFeS under photothermal conditions is 1.576 V, only 8 mV lower than under dark conditions, indicating that the photothermal response capability of pure NiFeS is limited. In contrast, the NiFeS/$Cs_{0.32}WO_3$-60 mg composite exhibits a potential reduction of 31 mV under photothermal conditions, which is 3.9 times that of NiFeS, demonstrating that $Cs_{0.32}WO_3$ is a crucial photothermal component for enhancing photothermal-assisted electrocatalytic performance. To more clearly compare the catalytic activities of various samples, Figure 5b shows the overpotentials of different catalysts at a current density of 50 mA $cm^{-2}$. Under dark conditions, the overpotential of NiFeS is 355 mV, while that of the NiFeS/$Cs_{0.32}WO_3$-60 mg composite decreases to 332 mV. Upon introduction of the photothermal effect, the overpotential of NiFeS/$Cs_{0.32}WO_3$-60 mg further decreases t to 301 mV. It is noteworthy that excessive $Cs_{0.32}WO_3$ loading (200 mg) actually decreases the catalytic activity, which is attributed to excessive $Cs_{0.32}WO_3$ covering the active sites of NiFeS, indicating the existence of an optimal composite ratio. Figure 5c shows the Tafel plots of various samples, used to evaluate OER kinetics. The Tafel slope of NiFeS under photothermal conditions is 57.8 mV $dec^{-1}$, while that of the NiFeS/$Cs_{0.32}WO_3$-60 mg composite under photothermal conditions decreases to 44.5 mV $dec^{-1}$. This indicates that the OER kinetics of the composite are faster under photothermal assistance. Figure 5d shows the Nyquist plots of NiFeS and NiFeS/$Cs_{0.32}WO_3$-60 mg composite under dark and photothermal conditions, with the inset showing the equivalent circuit model (Table S1). Fitting results show that the Rct values of NiFeS under dark and photothermal conditions are 10.4 Ω and 6.0 Ω, respectively, while those of the NiFeS/$Cs_{0.32}WO_3$-60 mg composite are 4.4 Ω and 3.0 Ω, respectively. From NiFeS under dark conditions (10.4 Ω) to NiFeS/$Cs_{0.32}WO_3$-60 mg under dark conditions (4.4 Ω), Rct decreases by 6.0 Ω, which is attributed to interfacial electron transfer at the heterostructure optimizing the charge transport pathway; from NiFeS/$Cs_{0.32}WO_3$-60 mg under dark conditions (4.4 Ω) to photothermal conditions (3.0 Ω), Rct further decreases by 1.4 Ω, which originates from the photothermal effect accelerating charge transfer at the electrode/electrolyte interface. Additionally, the double-layer capacitance (Cdl) of the samples at different scan rates (20–120 mV $s^{-1}$) was determined by cyclic voltammetry to evaluate the electrochemical active surface area (ECSA) of the catalysts (Figure S2). As shown in Figure S2, the Cdl

values of NiFeS, NiFeS/$Cs_{0.32}WO_3$-60 mg, and NiFeS/$Cs_{0.32}WO_3$-200 mg are 96.9, 309.1, and 211.6 μF $cm^{-2}$, respectively. This indicates that the introduction of an appropriate amount of $Cs_{0.32}WO_3$ can increase the electrochemical active surface area of the catalyst, exposing more catalytically active sites. However, excessive $Cs_{0.32}WO_3$ doping (200 mg) causes a decrease in Cdl value, which is due to excessive $Cs_{0.32}WO_3$ accumulation covering some of the active sites of NiFeS, consistent with the OER performance analysis results.

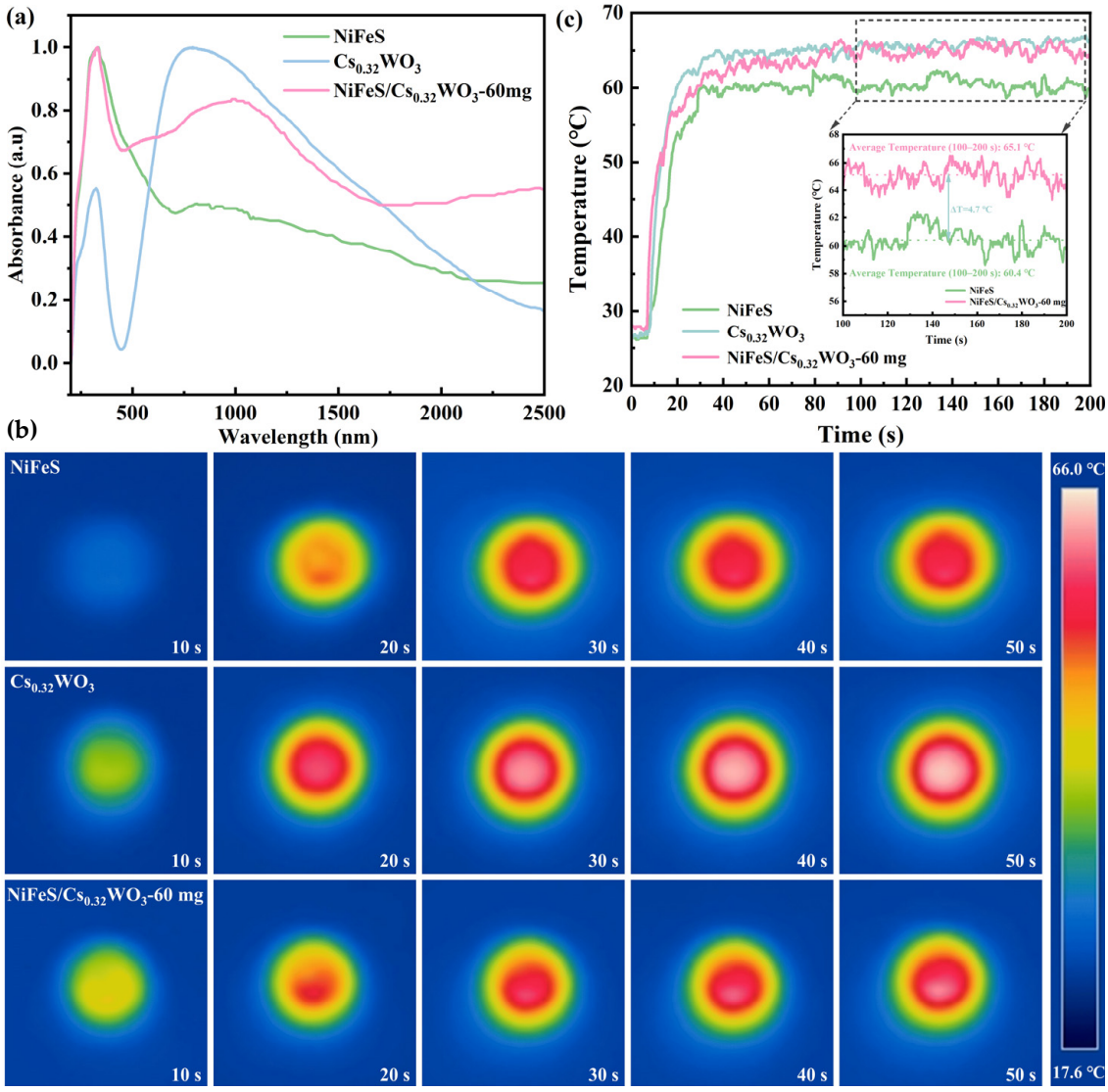


**Figure 4.** (**a**) UV-vis diffuse reflectance spectra (200–2500nm); (**b**) infrared thermal images of NiFeS, $Cs_{0.32}WO_3$ and NiFeS/$Cs_{0.32}WO_3$-60 mg under 808 nm laser irradiation; (**c**) temperature–time curves (inset: average temperature comparison during 100–200 s).

To further investigate the electron transfer mechanism of the NiFeS/$Cs_{0.32}WO_3$ heterostructure, UV-vis diffuse reflectance spectroscopy (DRS), ultraviolet photoelectron spectroscopy (UPS), and X-ray photoelectron spectroscopy valence band (XPS-VB) spectra were employed to determine the optical band gap (Eg), work function (Φ), and valence band edge (eV) of NiFeS and $Cs_{0.32}WO_3$, respectively. As shown in Figure 6a,d, the secondary electron cutoff (SEC) values of NiFeS and $Cs_{0.32}WO_3$ are 17.44 and 17.11 eV, respectively. According to the formula $\Phi = h\nu - SEC$, with the excitation source radiation energy of 21.22 eV ($h\nu$ = 21.22 eV), the calculated work functions are $\Phi_1$ = 4.11 eV for $Cs_{0.32}WO_3$ and $\Phi_2$ = 3.78 eV for NiFeS. As shown in Figure 6b,e, the positions of the valence band

maximum relative to the Fermi level were determined by linear extrapolation of the XPS-VB spectra, with ΔEV values of 1.14 and 2.38 eV for NiFeS and $Cs_{0.32}WO_3$, respectively. As shown in Figure 6c,f, the band gaps are Eg1 = 2.83 eV for $Cs_{0.32}WO_3$ and Eg2 = 2.05 eV for NiFeS. Based on the above DRS, UPS, and XPS-VB analysis results, the energy band structure diagrams of NiFeS and $Cs_{0.32}WO_3$ were constructed (Figure 6g). Before contact, since the work function of $Cs_{0.32}WO_3$ (4.11 eV) is higher than that of NiFeS (3.78 eV), the Fermi level of $Cs_{0.32}WO_3$ is lower relative to the vacuum level. When the two materials come into contact to form a heterostructure (Figure 6h), due to the difference in Fermi levels, electrons will spontaneously flow from NiFeS with the higher Fermi level to $Cs_{0.32}WO_3$ with the lower Fermi level until equilibrium of their Fermi levels is achieved. The above energy band analysis results are mutually corroborated the XPS characterization results. This interfacial electron transfer effect optimizes the electronic structure of the catalyst, reducing the electron cloud density at NiFeS active sites, which is favorable for the adsorption and conversion of oxygen-containing intermediates (OH*, O*, OOH*) during the OER process, thereby enhancing electrocatalytic activity.

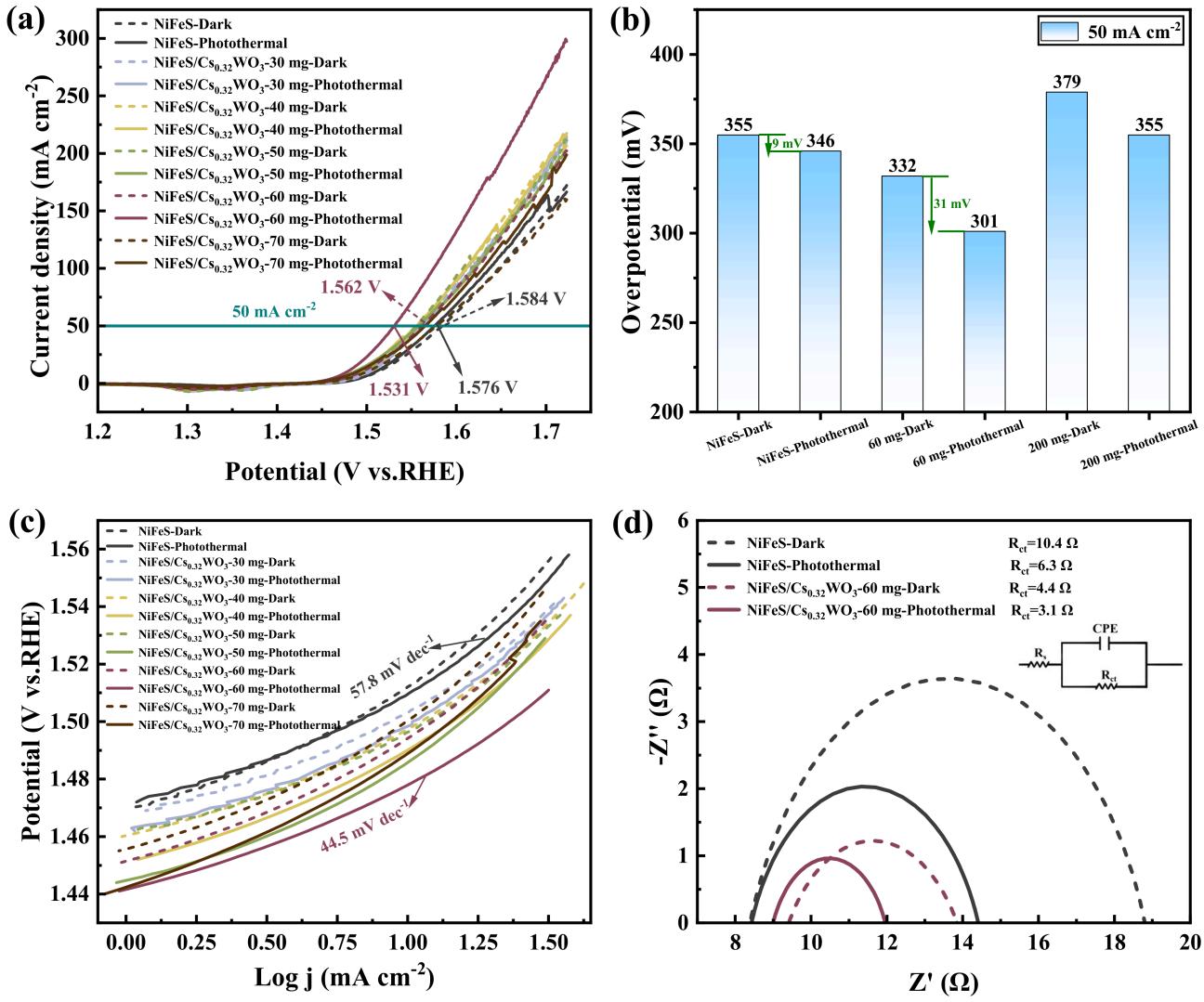


**Figure 5.** Electrocatalytic OER performance of NiFeS and NiFeS/$Cs_{0.32}WO_3$ composites under dark and photothermal conditions: (**a**) LSV curves; (**b**) overpotential comparison at 50 mA $cm^{-2}$; (**c**) Tafel plots; (**d**) EIS plots (inset: equivalent circuit model).

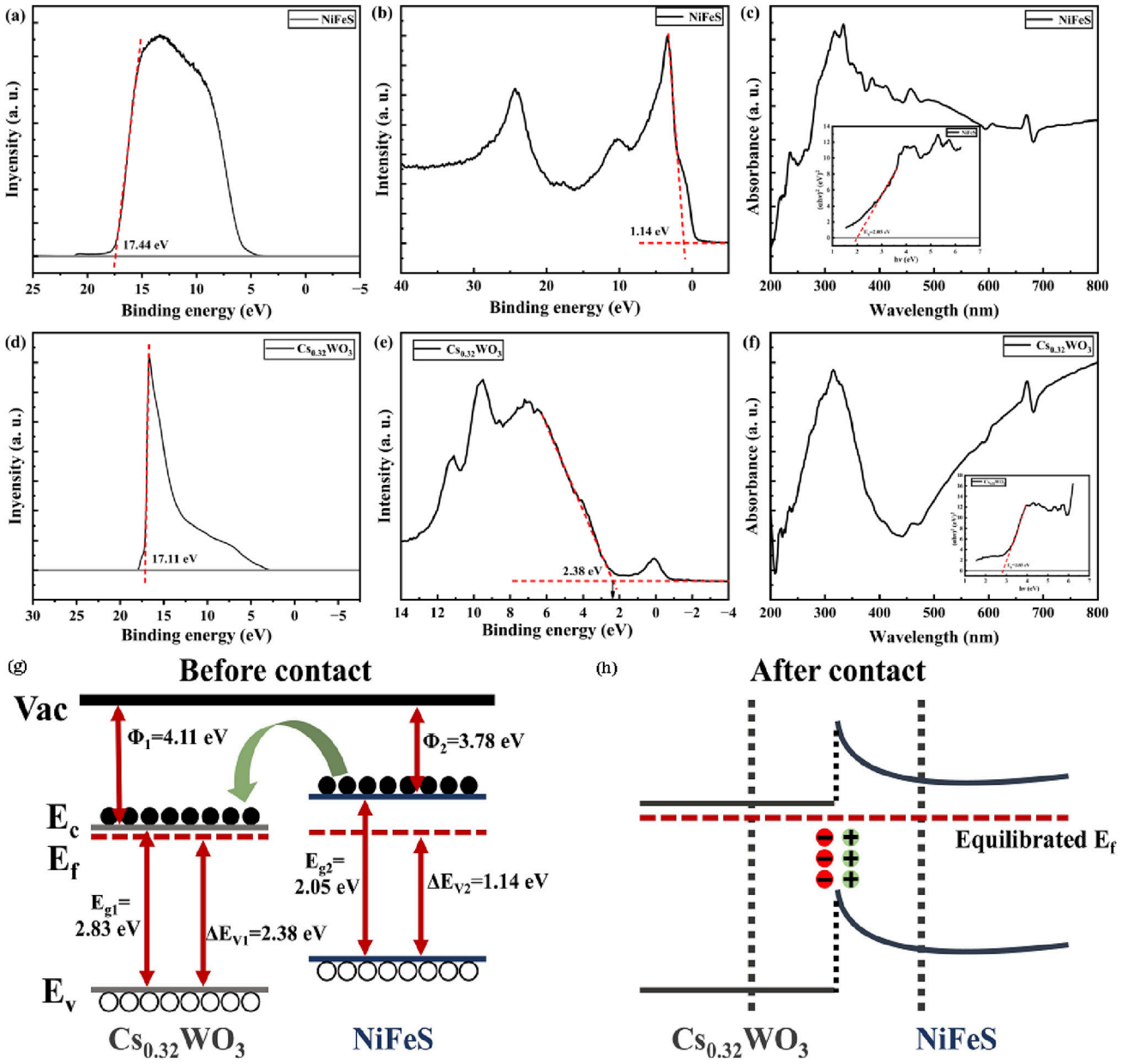


**Figure 6.** (**a**,**d**) UPS secondary electron cutoff spectra; (**b**,**e**) XPS valence band spectra; (**c**,**f**) UV-vis diffuse reflectance spectra (insets: Tauc plots); (**g**) schematic band structure before contact; (**h**) band structure and electron transfer after contact.

## 3. Materials and Methods

### *3.1. Materials*

Terephthalic acid (PTA, 99.0%), nickel chloride hexahydrate ($NiCl_2 \cdot 6H_2O$, analytical reagent, ≥98.0%), sodium sulfide ($Na_2S$, ≥95.0%), N,N-dimethylformamide (DMF, ≥99.5%), tungsten hexachloride ($WCl_6$, 99%), cesium hydroxide monohydrate ($CsOH \cdot H_2O$, analytical reagent), glacial acetic acid ($CH_3COOH$, analytical reagent), and Nafion D-521 dispersion (5 wt%) were all purchased from Shanghai Aladdin Biochemical Technology Co., Ltd. (Shanghai, China). Iron(III) chloride hexahydrate ($FeCl_3 \cdot 6H_2O$, analytical reagent) was purchased from Fuchen Chemical Reagent Co., Ltd. (Tianjin, China). Anhydrous ethanol ($C_2H_5OH$, analytical reagent) was supplied by Chengdu Jinshan Chemical Reagent Co., Ltd. (Chengdu, China). All chemical reagents were of analytical grade and used without further purification. Deionized water with a resistivity of 18.25 MΩ·cm,

prepared using a Youpu ultrapure water system (UPR-II-10TNZ, Sichuan, China), was used throughout all experiments.

### *3.2. Preparation of $Cs_{0.32}WO_3$*

First, 0.18 g of $CsOH{\cdot}H_2O$ was dissolved in 32 mL of anhydrous ethanol under magnetic stirring at room temperature until complete dissolution, followed by the addition of 1.28 g of $WCl_6$ with continued stirring until the solution became clear. Under continuous stirring, 8 mL of glacial acetic acid was slowly added dropwise and mixed thoroughly. The resulting precursor solution was transferred into a 100 mL Teflon-lined autoclave, which was then sealed and placed in an oven for hydrothermal treatment at 230 °C for 24 h. After the autoclave was naturally cooled to room temperature, the product was collected and washed alternately with deionized water and anhydrous ethanol three times by centrifugation, followed by vacuum drying at 60 °C for 12 h to obtain $Cs_{0.32}WO_3$ powder.

### *3.3. Preparation of NiFeS*

First, a solvent system was prepared by mixing 32 mL of DMF, 2 mL of anhydrous ethanol, and 2 mL of deionized water. Subsequently, 1.6 mmol of PTA, 2.4 mmol of $NiCl_2{\cdot}6H_2O$, 0.6 mmol of $FeCl_3{\cdot}6H_2O$, and 0.6 mmol of $Na_2S$ were added to the above mixed solvent and subjected to ultrasonication for 30 min to achieve thorough dispersion. The obtained precursor solution was transferred into a 100 mL Teflon-lined autoclave, which was then sealed and maintained at 200 °C for 10 h. After the reaction was completed, the autoclave was naturally cooled to room temperature, the precipitate was collected and washed alternately with deionized water and anhydrous ethanol three times by centrifugation. The final product was dried in a vacuum oven at 60 °C for 12 h to obtain NiFeS powder samples.

### *3.4. Preparation of NiFeS/$Cs_{0.32}WO_3$*

The preparation process of NiFeS/$Cs_{0.32}WO_3$ composite was similar to that of NiFeS, except that a certain amount of pre-synthesized $Cs_{0.32}WO_3$ powder was added to the precursor solution. After ultrasonication for 30 min, the mixture was transferred into a 100 mL Teflon-lined autoclave and maintained at 200 °C for 10 h. After natural cooling to room temperature, the product was washed alternately with deionized water and anhydrous ethanol three times by centrifugation, followed by vacuum drying at 60 °C for 12 h to obtain the NiFeS/$Cs_{0.32}WO_3$ composite.

### *3.5. Characterizations*

The crystal structure of the samples was characterized using a Bruker D8 Advance X-ray powder diffractometer (Bruker, Bremen, Germany) with Cu Kα radiation (λ = 1.54059 Å), scanning range of 5° to 80°, and scanning rate of 5°/min. The microstructure and lattice structure of the samples were observed using a field emission transmission electron microscope ("FEI Talos F200X, Hillsboro, OR, USA). The elemental composition and chemical states of the samples were analyzed using an X-ray photoelectron spectrometer (XPS, Thermo Scientific Escalab 250Xi, Waltham, MA, USA), with all binding energies calibrated against adventitious carbon at C 1s = 284.8 eV. The optical absorption properties of the samples were measured using a UV–visible diffuse reflectance spectrometer (UV-vis DRS, Shimadzu UV-3600, Kyoto, Japan) equipped with an integrating sphere attachment, using $BaSO_4$ as the reference. Photothermal conversion of the samples under near-infrared irradiation was recorded using an infrared thermal imaging camera (808 nm, 5 W).

### *3.6. Electrocatalytic Performance Testing*

All electrochemical measurements were performed on a CHI660E electrochemical workstation using a standard three-electrode system, with a glassy carbon electrode (GCE, diameter 3 mm) as the working electrode, a mercury/mercury oxide electrode (Hg/HgO) as the reference electrode, a graphite rod as the counter electrode, and 1 M KOH solution as the electrolyte. Prior to formal testing, the electrodes were activated by cyclic voltammetry (CV) for 10 cycles in the potential range of 0 to 0.8 V at a scan rate of 100 mV $s^{-1}$ to obtain stable electrochemical signals. Linear sweep voltammetry (LSV) was employed to evaluate the oxygen evolution reaction (OER) activity of the catalysts, with a potential range of 0 to 0.8 V, scan rate of 5 mV $s^{-1}$, and reverse scanning mode. Electrochemical impedance spectroscopy (EIS) measurements were conducted at the potential corresponding to a current density of 10 mA $cm^{-2}$, with a frequency range of 100 kHz to 1 Hz. Photoelectrocatalytic experiments employed a JH-GHX300 xenon lamp light source (Jihui Analytical Instrument Co., Shanghai, China) as the simulated light source, with an operating current of 15 A and power specifications of AC 220 V, 50 Hz. Measurements were performed under both dark and illuminated conditions; during dark measurements, the electrolytic cell was covered with a black light-blocking shield, while during illuminated measurements, the light source was directed onto the surface of the L-shaped working electrode in an optical water-bath circulating electrolytic cell, with a circulating water cooling system maintaining constant electrolyte temperature to eliminate the influence of electrolyte heating on the test results.

## 4. Conclusions

In this study, NiFeS/$Cs_{0.32}WO_3$ heterostructure composites were successfully prepared via a solvothermal method. $Cs_{0.32}WO_3$ possesses a unique hexagonal tungsten bronze structure, and the LSPR effect endows the composite with excellent near-infrared light absorption performance. Since the work function of $Cs_{0.32}WO_3$ (4.11 eV) is higher than that of NiFeS (3.78 eV), electrons spontaneously transfer from NiFeS to $Cs_{0.32}WO_3$ upon contact, forming a built-in electric field at the interface; this electron transfer behavior was confirmed by XPS, showing that the Fe 2p binding energy shifts positively by 0.72 eV after compositing, while the Cs 3d and W 4f binding energies shift negatively by 0.14 eV and 0.26 eV, respectively. The NiFeS/$Cs_{0.32}WO_3$-60 mg composite exhibits excellent catalytic activity in the photothermal-assisted electrocatalytic OER process, with an overpotential of only 301 mV at a current density of 50 mA $cm^{-2}$ and a Tafel slope of 44.5 mV $dec^{-1}$. Compared to NiFeS under dark conditions, the composite exhibits a potential reduction of 53 mV under photothermal conditions; the enhanced overall performance of the NiFeS/$Cs_{0.32}WO_3$ composite is primarily attributed to its photothermal enhancement effect, whereas the intrinsic interfacial effects arising from the heterojunction also contribute significantly and cannot be neglected. The performance enhancement can be attributed to the photothermal conversion effect of $Cs_{0.32}WO_3$ accelerating the charge transfer kinetics at the electrode/electrolyte interface, while interfacial electron transfer at the heterostructure optimizes the electronic structure of the catalyst. The heterostructure–photothermal synergistic enhancement mechanism revealed in this study can provide insights for the design of efficient electrocatalytic materials in the field of clean energy.

**Supplementary Materials:** The following supporting information can be downloaded at: https://www.mdpi.com/article/10.3390/molecules31132330/s1, Figure S1: EDS line scan analysis of NiFeS/$Cs_{0.32}WO_3$-60 mg composite: (a) TEM image showing the line scan region; (b) overview of elemental signal intensities; (c–h) line scan intensity profiles of Ni, Fe, S, Cs, W and O elements; Figure S2: Double-layer capacitance (Cdl) measurements of NiFeS and NiFeS/$Cs_{0.32}WO_3$ composites: CV curves of (a) NiFeS, (b) NiFeS/$Cs_{0.32}WO_3$-60 mg and (c) NiFeS/$Cs_{0.32}WO_3$-200 mg at different scan

rates (20–120 mV s−1); (d) Cdl fitting curves; Figure S3: Stability test of NiFeS/$Cs_{0.32}WO_3$-60 mg composite; Table S1: Solution resistance ($R_s$), charge-transfer resistance ($R_{ct}$), and corresponding fitting errors for all samples.

**Author Contributions:** Conceptualization: S.W. and Z.W.; Methodology: Z.W. and X.Z.; Validation: X.Z., W.W. and X.S.; Formal analysis: Z.W., X.Z. and W.W.; Investigation: Z.W. and X.S.; Resources: X.Y. and S.W.; Data Curation: Z.W. and S.W.; Writing—Original Draft: Z.W. and X.Z.; Writing—Review and Editing: X.Y. and S.W.; Visualization: Z.W. and X.Z.; Supervision: S.W.; Project administration: S.W.; Funding acquisition: S.W. All authors have read and agreed to the published version of the manuscript.

**Funding:** This research was supported by the National Key R&D Program of China (Grant No. 2023YFB3813300), Science and Technology Program of Xizang Autonomous Region (Grant Nos. XZ202402JD0001 and XZ202401YD0004), Open Competition Program of Xizang Autonomous Region (Grant No. XZ202403ZY0016), High-level Talent Program Project of Xizang Autonomous Region (Grant No. 00061422), and Talent Innovation Team and Laboratory Platform Construction Project of Xizang University (No. 00061403 and 00061411).

**Institutional Review Board Statement:** Not applicable.

**Informed Consent Statement:** Not applicable.

**Data Availability Statement:** The original contributions presented in this study are included in the article/Supplementary Materials. Further inquiries can be directed to the corresponding author.

**Conflicts of Interest:** The authors declare no conflicts of interest.

## References

1. Yu, M.; Budiyanto, E.; Tüysüz, H. Principles of Water Electrolysis and Recent Progress in Cobalt-, Nickel-, and Iron-Based Oxides for the Oxygen Evolution Reaction. *Angew. Chem. Int. Ed.* **2022**, *61*, e202103824.
2. Jiao, S.; Fu, X.; Wang, S.; Zhao, Y. Perfecting Electrocatalysts via Imperfections: Towards the Large-Scale Deployment of Water Electrolysis Technology. *Energy Environ. Sci.* **2021**, *14*, 1722–1770.
3. Song, J.; Wei, C.; Huang, Z.-F.; Liu, C.; Zeng, L.; Wang, X.; Xu, Z.J. A Review on Fundamentals for Designing Oxygen Evolution Electrocatalysts. *Chem. Soc. Rev.* **2020**, *49*, 2196–2214. [CrossRef] [PubMed]
4. Suen, N.-T.; Hung, S.-F.; Quan, Q.; Zhang, N.; Xu, Y.-J.; Chen, H.M. Electrocatalysis for the Oxygen Evolution Reaction: Recent Development and Future Perspectives. *Chem. Soc. Rev.* **2017**, *46*, 337–365. [CrossRef] [PubMed]
5. Seh, Z.W.; Kibsgaard, J.; Dickens, C.F.; Chorkendorff, I.; Nørskov, J.K.; Jaramillo, T.F. Combining Theory and Experiment in Electrocatalysis: Insights into Materials Design. *Science* **2017**, *355*, eaad4998. [CrossRef] [PubMed]
6. Guo, Y.; Park, T.; Yi, J.W.; Henzie, J.; Kim, J.; Wang, Z.; Jiang, B.; Bando, Y.; Sugahara, Y.; Tang, J.; et al. Nanoar chitectonics for Transition-Metal-Sulfide-Based Electrocatalysts for Water Splitting. *Adv. Mater.* **2019**, *31*, 1807134.
7. Man, I.C.; Su, H.-Y.; Calle-Vallejo, F.; Hansen, H.A.; Martínez, J.I.; Inoglu, N.G.; Kitchin, J.; Jaramillo, T.F.; Nørskov, J.K.; Rossmeisl, J. Universality in Oxygen Evolution Electrocatalysis on Oxide Surfaces. *ChemCatChem* **2011**, *3*, 1159–1165. [CrossRef]
8. Kawashima, K.; Marquez, R.A.; Smith, L.A.; Vaidyula, R.R.; Carrasco-Jaim, O.A.; Wang, Z.; Son, Y.J.; Cao, C.L.; Mullins, C.B. A Review of Transition Metal Boride, Carbide, Pnictide, and Chalcogenide Water Oxidation Electrocatalysts. *Chem. Rev.* **2023**, *123*, 12795–13208. [CrossRef] [PubMed]
9. Sun, L.; Luo, Q.; Dai, Z.; Ma, F. Material Libraries for Electrocatalytic Overall Water Splitting. *Coord. Chem. Rev.* **2021**, *444*, 214049. [CrossRef]
10. Xu, H.; Shang, H.; Wang, C.; Du, Y. Surface and Interface Engineering of Noble-Metal-Free Electrocatalysts for Efficient Overall Water Splitting. *Coord. Chem. Rev.* **2020**, *418*, 213374.
11. Li, X.-P.; Huang, C.; Han, W.-K.; Ouyang, T.; Liu, Z.-Q. Transition Metal-Based Electrocatalysts for Overall Water Splitting. *Chin. Chem. Lett.* **2021**, *32*, 2597–2616. [CrossRef]
12. Peng, L.; Yang, N.; Yang, Y.; Wang, Q.; Xie, X.; Sun-Waterhouse, D.; Shang, L.; Zhang, T.; Waterhouse, G.I. Atomic Cation-Vacancy Engineering of NiFe-Layered Double Hydroxides for Improved Activity and Stability towards the Oxygen Evolution Reaction. *Angew. Chem. Int. Ed.* **2021**, *60*, 24612–24619.
13. Xue, Z.-H.; Su, H.; Yu, Q.-Y.; Zhang, B.; Wang, H.-H.; Li, X.-H.; Chen, J.-S. Janus Co/CoP Nanoparticles as Efficient Mott–Schottky Electrocatalysts for Overall Water Splitting in Wide pH Range. *Adv. Energy Mater.* **2017**, *7*, 1602355.

14. Zhao, G.; Rui, K.; Dou, S.X.; Sun, W. Heterostructures for Electrochemical Hydrogen Evolution Reaction: A Review. *Adv. Funct. Mater.* **2018**, *28*, 1803291. [CrossRef]
15. Li, Z.; Hu, M.; Wang, P.; Liu, J.; Yao, J.; Li, C. Heterojunction Catalyst in Electrocatalytic Water Splitting. *Coord. Chem. Rev.* **2021**, *439*, 213953. [CrossRef]
16. Peng, L.; Su, L.; Yu, X.; Wang, R.; Cui, X.; Tian, H.; Cao, S.; Xia, B.Y.; Shi, J. Electron Redistribution of Ruthenium-Tungsten Oxides Mott-Schottky Heterojunction for Enhanced Hydrogen Evolution. *Appl. Catal. B Environ.* **2022**, *308*, 121229.
17. Wang, N.; Ning, S.; Yu, X.; Chen, D.; Li, Z.; Xu, J.; Meng, H.; Zhao, D.; Li, L.; Liu, Q.; et al. Graphene Composites with Ru-$RuO_2$ Heterostructures: Highly Efficient Mott–Schottky-Type Electrocatalysts for pH-Universal Water Splitting and Flexible Zinc–Air Batteries. *Appl. Catal. B Environ.* **2022**, *302*, 120838.
18. Gu, C.; Zhou, G.; Yang, J.; Pang, H.; Zhang, M.; Zhao, Q.; Gu, X.; Tian, S.; Zhang, J.; Xu, L.; et al. NiS/$MoS_2$ Mott-Schottky Heterojunction-Induced Local Charge Redistribution for High-Efficiency Urea-Assisted Energy-Saving Hydrogen Production. *Chem. Eng. J.* **2022**, *443*, 136321.
19. Wen, Q.; Yang, K.; Huang, D.; Cheng, G.; Ai, X.; Liu, Y.; Fang, J.; Li, H.; Yu, L.; Zhai, T. Schottky Heterojunction Nanosheet Array Achieving High-Current-Density Oxygen Evolution for Industrial Water Splitting Electrolyzers. *Adv. Energy Mater.* **2021**, *11*, 2102353.
20. Zhong, Y.; Chang, B.; Shao, Y.; Xu, C.; Wu, Y.; Hao, X. Regulating Phase Conversion from $Ni_3Se_2$ into NiSe in a Bifunctional Electrocatalyst for Overall Water-Splitting Enhancement. *ChemSusChem* **2019**, *12*, 2008–2014. [PubMed]
21. Li, T.; Yin, J.; Sun, D.; Zhang, M.; Pang, H.; Xu, L.; Zhang, Y.; Yang, J.; Tang, Y.; Xue, J. Manipulation of Mott- Schottky Ni/$CeO_2$ Heterojunctions into N-Doped Carbon Nanofibers for High-Efficiency Electrochemical Water Splitting. *Small* **2022**, *18*, 2106592.
22. Zhang, P.; Liu, Y.; Liang, T.; Ang, E.H.; Zhang, X.; Ma, F.; Dai, Z. Nitrogen-Doped Carbon Wrapped Co-Mo2C Dual Mott–Schottky Nanosheets with Large Porosity for Efficient Water Electrolysis. *Appl. Catal. B Environ.* **2021**, *284*, 119738.
23. Zhang, Q.; Luo, F.; Long, X.; Yu, X.; Qu, K.; Yang, Z. N, P Doped Carbon Nanotubes Confined WN-Ni Mott-Schottky Heterogeneous Electrocatalyst for Water Splitting and Rechargeable Zinc-Air Batteries. *Appl. Catal. B Environ.* **2021**, *298*, 120511.
24. Yao, J.; Huang, W.; Fang, W.; Kuang, M.; Jia, N.; Ren, H.; Liu, D.; Lv, C.; Liu, C.; Xu, J.; et al. Promoting Electro catalytic Hydrogen Evolution Reaction and Oxygen Evolution Reaction by Fields: Effects of Electric Field, Magnetic Field, Strain, and Light. *Small Methods* **2020**, *4*, 2000494.
25. Fang, S.; Hu, Y.H. Thermo-Photo Catalysis: A Whole Greater than the Sum of Its Parts. *Chem. Soc. Rev.* **2022**, *51*, 3609–3647. [CrossRef] [PubMed]
26. Garcés-Pineda, F.A.; Blasco-Ahicart, M.; Nieto-Castro, D.; López, N.; Galán-Mascarós, J.R. Direct Magnetic Enhancement of Electrocatalytic Water Oxidation in Alkaline Media. *Nat. Energy* **2019**, *4*, 519–525. [CrossRef]
27. Ai, L.; Chen, M.; Luo, Y.; Tian, Y.; Wang, X.; Wei, W.; Jiang, J. One-Pot Corrosive Synthesis of Ru-$Fe_3O_4$ Hetero structure: A Localized Photothermal Electrocatalyst towards Accelerated Water Splitting. *Colloids Surf. Physicochem. Eng. Asp.* **2022**, *651*, 129767.
28. Shi, Y.; Wang, J.; Wang, C.; Zhai, T.-T.; Bao, W.-J.; Xu, J.-J.; Xia, X.-H.; Chen, H.-Y. Hot Electron of Au Nanorods Activates the Electrocatalysis of Hydrogen Evolution on $MoS_2$ Nanosheets. *J. Am. Chem. Soc.* **2015**, *137*, 7365–7370. [CrossRef] [PubMed]
29. Zhang, Y.; Wang, Y.; Jiang, H.; Huang, M. Multifunctional Nickel Sulfide Nanosheet Arrays for Solar-Intensified Oxygen Evolution Reaction. *Small* **2020**, *16*, 2002550.
30. Ai, L.; Li, N.; Chen, M.; Jiang, H.; Jiang, J. Photothermally Boosted Water Splitting Electrocatalysis by Broadband Solar Harvesting Nickel Phosphide within a Quasi-MOF. *J. Mater. Chem. A* **2021**, *9*, 16479–16488. [CrossRef]
31. Jin, B.; Li, Y.; Wang, J.; Meng, F.; Cao, S.; He, B.; Jia, S.; Wang, Y.; Li, Z.; Liu, X. Promoting Oxygen Evolution Reaction of Co-Based Catalysts ($Co_3O_4$, CoS, CoP, and CoN) through Photothermal Effect. *Small* **2019**, *15*, 1903847.
32. Wu, X.; Wang, J.; Wang, Z.; Sun, F.; Liu, Y.; Wu, K.; Meng, X.; Qiu, J. Boosting the Electrocatalysis of MXenes by Plasmon-Induced Thermalization and Hot-Electron Injection. *Angew. Chem. Int. Ed.* **2021**, *60*, 9416–9420.
33. Wang, S.-S.; Jiao, L.; Qian, Y.; Hu, W.-C.; Xu, G.-Y.; Wang, C.; Jiang, H.-L. Boosting Electrocatalytic Hydrogen Evolution over Metal–Organic Frameworks by Plasmon-Induced Hot-Electron Injection. *Angew. Chem.* **2019**, *131*, 10823–10827.
34. Gao, L.; Cui, X.; Wang, Z.; Sewell, C.D.; Li, Z.; Liang, S.; Zhang, M.; Li, J.; Hu, Y.; Lin, Z. Operando Unraveling Photothermal-Promoted Dynamic Active-Sites Generation in $NiFe_2O_4$ for Markedly Enhanced Oxygen Evolution. *Proc. Natl. Acad. Sci. USA* **2021**, *118*, e2023421118. [PubMed]
35. Gu, L.; Zhang, C.; Guo, Y.; Gao, J.; Yu, Y.; Zhang, B. Enhancing Electrocatalytic Water Splitting Activities via Photothermal Effect over Bifunctional Nickel/Reduced Graphene Oxide Nanosheets. *ACS Sustain. Chem. Eng.* **2019**, *7*, 3710–3714. [CrossRef]
36. Hao, W.; Wu, R.; Yang, H.; Guo, Y. Photothermal Coupling Electrolysis on Ni–W–B toward Practical Overall Water Splitting. *J. Mater. Chem. A* **2019**, *7*, 12440–12445.
37. Yao, D.; Hao, W.; Weng, S.; Hou, M.; Cen, W.; Li, G.; Chen, Z.; Li, Y. Local Photothermal Effect Enabling $N_{i3}Bi_2S_2$ Nanoarray Efficient Water Electrolysis at Large Current Density. *Small* **2022**, *18*, 2106868.

38. Nakakura, S.; Arif, A.F.; Machida, K.; Adachi, K.; Ogi, T. Cationic Defect Engineering for Controlling the Infrared Absorption of Hexagonal Cesium Tungsten Bronze Nanoparticles. *Inorg. Chem.* **2019**, *58*, 9101–9107. [CrossRef] [PubMed]
39. Guo, C.; Yin, S.; Yan, M.; Kobayashi, M.; Kakihana, M.; Sato, T. Morphology-Controlled Synthesis of $W_{18}O_{49}$ Nanostructures and Their near-Infrared Absorption Properties. *Inorg. Chem.* **2012**, *51*, 4763–4771. [PubMed]
40. Yang, L.; Wang, M.; Shan, H.; Ma, Y.; Peng, Y.; Hu, K.; Deng, C.; Yu, H.; Lv, J. Generic Heterostructure Interfaces Bound to $Co_9S_8$ for Efficient Overall Water Splitting Supported by Photothermal. *J. Colloid Interface Sci.* **2024**, *662*, 748–759. [CrossRef] [PubMed]
41. Liu, Q.; Wang, J.; Zhang, Y.; Gao, W.; Cui, L.; Low, J.; Zhang, H. Solar-Boosted Electrocatalytic Oxygen Evolution via a 2D/2D Heterostructure Constructed by Integrating Reduced Graphene Oxide on NiFe-LDH Nanosheets. *Mater. Today Phys.* **2025**, *50*, 101619.